# Understanding Enzyme Kinetics on Coacervate as a Substrate Hub

Zhicheng Jin, a Jesse V. Jokersta, b, c,\*

<sup>a</sup>Department of NanoEngineering, University of California, San Diego, La Jolla, CA 92093; <sup>b</sup>Materials Science and Engineering Program, University of California, San Diego, La Jolla, CA 92093; <sup>c</sup>Department of Radiology, University of California, San Diego, La Jolla, CA 92093; \*Corresponding author's email: jjokerst@ucsd.edu (J.V.J.)

#### **ABSTRACT**

There remains a gap in understanding the enzyme interactions with the coacervate as a substrate hub. Here, we study how the hydrophobicity nature of coacervate affects the interactions of the embedded substrate with a protease. We design oligopeptide-based coacervates that comprise an anionic Asp-peptide ( $D_{10}$ ) and a cationic Arg-peptide ( $R_5R_5$ ) with a proteolytic cleavage site. The coacervates dissolve when exposed to the main protease. We exploit the condensed structure, implement a self-quenching mechanism, and characterize enzyme kinetics with Cy5.5-labeled peptides. The determined specificity constant is 5,817  $M^{-1}$  s<sup>-1</sup> and is similar to that of the free substrate. We further show that the enzyme kinetics depend on the amount of dye incorporated into the coacervates. Our work presents a simple design for coacervates with tuned bioactivities and provides insights into the kinetics between the enzyme and coacervates as a substrate hub.

Keywords: Peptide coacervates, bioactivity, enzyme kinetics, energy transfer, disassembly, hydrophobicity

# 1. INTRODUCTION

Membrane-less cellular organelles exhibit liquid-like properties due to biomolecular coalescence. These include stress granules and processing bodies (P-bodies) that recruit mRNA and RNA-binding proteins through liquid-liquid phase separation (LLPS).<sup>1-4</sup> Investigations into the fate of these organelles, as well as their responsive to stimuli such as pH,<sup>5</sup> redox potential,<sup>6</sup> light,<sup>7-8</sup> enzymes,<sup>9-10</sup> among others, could enhance the comprehension of important biological events including protein condensate formation,<sup>11-12</sup> substrate translocation,<sup>13</sup> and genomes regulation.<sup>10</sup> For example, condensed P-bodies are believed to physically protect the constituting mRNA from ribonuclease degradation, yet decay of specific substrate may still occur in these hubs.<sup>14-17</sup> This indicates the complex and elusive nature of the interactions between non-membrane organelles and enzymes.

Synthetic coacervates, which mimic membrane-free organelles, have gained significant attention for their ability to uncover the dynamics such as compartmentalization, 8-9, 18 mesostructured manipulations, 19-22 local reactions, 23-24 biomolecule transportation, 13 among others. Proteases are key participants in many biological events in cells, with proteolytic processing being critical to post modification, activity regulation, protein turnover, and signal transduction. *In vitro* evidence from Keating *et al.* have demonstrated that kinase and phosphatase can manipulate the reversible formation of coacervates by modifying the phosphorylation states and Coulombic interactions among the comprising peptides. Rosen *et al.* reported that the reversible LLPS of reconstituted chromatin droplets *in vivo* is histone tail-dependent, induced by histone acetyltransferase. These examples indicate that enzymes have a significant impact on the coacervate dynamics, nonetheless, the enzymatic kinetics on the condensed liquid-like substrate hub remain largely unexplored.

In this work, we present a simple system for modeling the proteolysis of complex coacervates. The coacervates were designed with oppositely charged peptides that coded a specific cleavage site, e.g.,  $D_{10}$  and  $R_5R_5$  peptides. We validated the system's response to the coronavirus main protease ( $M^{pro}$ ) in vitro. Upon cleaving the  $R_5R_5$  substrate,  $M^{pro}$  reduced the charge valence and weakened the electrostatic interactions, leading to the disassembly of the coacervates. To quantify the proteolytic kinetics, we introduced Cy5.5- $R_5R_5$  strand to the coacervates as optical reporters. A notable decrease in dye photoluminescence (PL) occurred through self-quenching within the droplets. However, the PL recovered in the presence of  $M^{pro}$ . We discovered that enzyme-coacervate interactions are influenced by droplet characteristics. Adding one dye-labeled strand minimally affects catalytic efficiency ( $k_{cat}/K_M$ ). Yet, labeling both strands with dye entirely prevents the protease from interacting with coacervates. Our results provide valuable insights into the

interactions between the protease and non-membrane coacervates and suggest a tunable bioactivity of coacervates for sensing and delivery applications.

# 2. RESULTS AND DISCUSSION

#### 2.1 Rationale

Our representative coacervates used  $R_5R_5$  and  $D_{10}$  peptides (**Figure 1a**). The modular cationic peptide has two charged (Arg)<sub>5</sub> termini flanking a specific M<sup>pro</sup> cleavage site, and the counterpart uses a decapeptide, (Asp)<sub>10</sub>. The prevalent electrostatic interactions between the two peptides yield complex coacervates because of the charge valence of 10 seen on the backbone from positive guanidine and negative carboxylate groups.<sup>26</sup> M<sup>pro</sup> is used as a model protease.<sup>27</sup> In **Figure 1b**, our hypothesis is that the endoproteolysis of cationic  $R_5R_5$  peptides would reduce their charge multivalency by half, thereby diminishing Columbic attractions and causing the dissolution of coacervates. Moreover, we employed dye-labeled peptides to construct optically addressable coacervates, which evaluate enzymatic kinetics via a self-quenching transduction mechanism (**Figure 1a**).

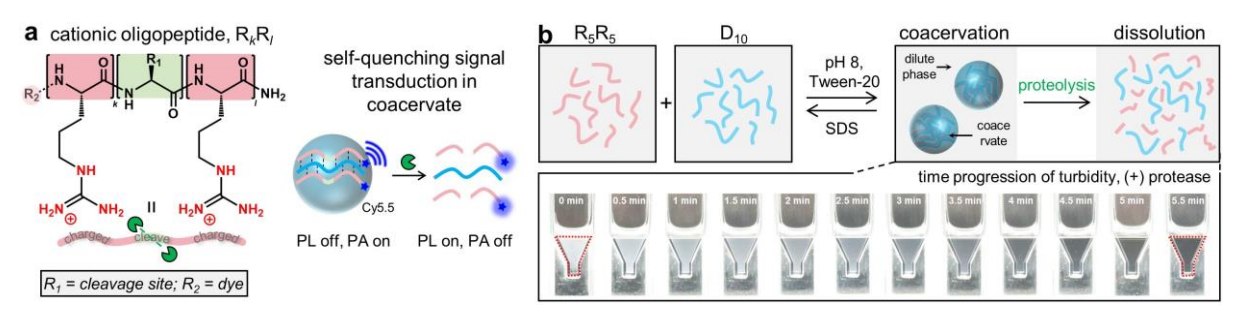


Figure 1. Protease-responsive oligopeptide-based coacervates. (a) Complex coacervates comprise of cationic Arg-rich oligopeptides, which have a cleavage site  $(R_1)$  and a free N-terminal amine for dye conjugation  $(R_2)$ . The confinement structure enables self-quenching signal transductions in coacervates. After proteolysis, photoluminescence (PL) recovers. (b) A mixture of  $R_5R_5$  and  $D_{10}$  at pH 8 results in a turbid emulsion containing the coacervates. Addition of the  $M^{pro}$  leads to a clear solution. The electrostatic interactions holding the coacervates can be broken by SDS surfactant.

# 2.2 Oligopeptide coacervates

The charge effects on complex coacervation were studied, including charge valence, charge density, and net charge. **Table 1** summarizes the peptides used in this work. For example, the cationic  $R_{10}$  decapeptide was derivatized to an  $R_k R_l$  formula (k, l-number of repeating unit) to encompass varying charge valency and a central  $M^{pro}$  cleavage sequence, AVLQ $\downarrow$ SGF. In **Figure 2a**, the mass spectrum (MS) of  $R_5R_5$  (*i.e.*, RRRRAVLQ $\downarrow$ SGFRRRR) showed a strong peak at 2282.9 that was attributed to its  $[M + H]^+$  ion (calcd 2280.4). Incubating  $R_5R_5$  with  $M^{pro}$  in phosphate buffer (20 mM, pH 8.0) at 37 °C for 1 h resulted in peaks at 1209.8 and 1088.6, ascribed to the  $[M + H]^+$  ion of the N-terminal (calcd 1209.8) and C-terminal fragments (calcd 1088.7), respectively. This suggests the successful synthesis of peptides and enzymatic cleavage. The MS of other substrates exhibited close alignment with the calculated values.

The anionic counterparts used  $D_{10}$  and  $D_5D_5$  peptides for coacervation. In addition, zwitterionic peptides were designed and synthesized such as  $R_{10}D_5$ ,  $R_{10}D_{10}$ , and  $R_5D_{10}$ , with varying net charges of +5, 0, and -5, respectively. Ion-pairing interactions arising from opposite charges on the mentioned peptide backbones drive the formation of complex coacervates.

We first evaluated the impact of *charge valence* on the coacervation of  $R_kR_l$  (k+l=5, 7, 10) with  $D_{10}$ . When combining oligopeptides with opposing charges, two results were observed: a transparent solution and an emulsion of coacervates. The conditions used 5 mM total charge, 0.5 charge ratio, 20 mM PB at pH 8, and 0.2% w/v Tween-20 unless otherwise indicated. In **Figure 2b**, the minimal charge valence for coacervation was found to be  $(k+l)_{min} = 10$  (second column), which also held true for  $D_5D_5$  (first column). For example, the coacervation occurred between combinations of ( $R_5R_5$ ,  $D_{10}$ ), ( $R_10$ ,  $D_{10}$ ), ( $R_20$ ,  $D_{10}$ ), ( $R_30$ ,  $D_30$ ), and ( $R_30$ ,  $D_{10}$ ), while  $R_20$ , and  $R_30$ 

**Table 1.** Information of the (dye-)oligopeptides for complex coacervation.

Effect		Peptide name	Peptide sequence [a]  (red-positive; green-cleavage; blue-negative)	M. W.[g/mol]	Net charge	Description	
arge	density	R <sub>2</sub> R <sub>3</sub>	RRAVLQ↓SGFRRR	1499.9	+5	cationic	
		R <sub>3</sub> R <sub>4</sub>	RRRAVLQ↓SGFRRRR	1813.1	+7	cationic	
ıcy, ch		R <sub>5</sub> R <sub>5</sub>	RRRRRAVLQ↓SGFRRRRR	2280.4	+10	cationic	
charge valency, charge		r5r5	RRRRRQ×FAGSLVRRRRR	2280.4	+10	cationic,	
		R <sub>10</sub>	RRRRRRRRR	1578.0	+10	cationic	
9	e .	R <sub>10</sub> D <sub>5</sub>	RRRRRRRRRAVLQ\\$GFDDDD	2855.5	+5	zwitterionic	
chore	net charge	$R_{10}D_{10}$	RRRRRRRRRAVLQ\\$GFDDDDDDDDDD	3430.6	0	zwitterionic	
por	ner	R <sub>5</sub> D <sub>10</sub>	RRRRAVLQ\\$GFDDDDDDDDD	2650.2	-5	zwitterionic	
charge	ity	D <sub>5</sub> D <sub>5</sub>	DDDDDAVLQ↓SGFDDDDD	1869.6	-10	anionic	
	density	$D_{10}$	DDDDDDDDD	1167.3	-10	anionic	
9	Silois	Cy5.5-R <sub>5</sub> R <sub>5</sub>	Cy5.5-RRRRRAVLQ↓SGFRRRRR	2850.7	+11	cationic, for self-quenching	
signs transductions	ı transduct	Cy3-R <sub>5</sub> R <sub>5</sub>	Cy3-RRRRRAVLQ↓SGFRRRR	2721.4 +11		cationic, for	
Gabia	Signa	Cy5.5-D <sub>10</sub>	Cy5.5-DDDDDDDDDD	1733.7	-9	anionic, for self-quenching	
molecular	probe	Cy5.5- R <sub>5</sub> R <sub>5</sub> -Cy3	Cy5.5-RRRRRAVLQ\\$GFRRRRC-Cy3	3528.1	+12	FRET probe	

<sup>[</sup>a] All peptides contain a free N-terminal amine and an amidated C-terminus; '\' designates the M<sup>pro</sup> cleavage site (coded in green); '×' designates non-cleavable sequence by M<sup>pro</sup>; NHS-ester dye was conjugated to the N-terminal amine; positively and negatively charged segment is coded in red and blue, respectively. [b] The electrophoretic property of peptide at pH 8.0, where the N-terminal amine is neutral in charge, and the Cy5.5 dye contributes to the net charge. <sup>29-30</sup>

aligns with Keating et al.'s discovery that peptidic polyions need to be at least 10 units long for coacervation, driven by a critical level of ion-pairing interactions.<sup>26</sup> This also suggests that the inner positioning of cleavage site in  $R_kR_l$  (e.g., at the center for  $R_5R_5$ ) is essential for the current design. It enables the intact coacervation of  $R_5R_5$  with  $D_{10}$ , while predicting the subsequent coacervate disassembly after endoproteolysis. Work from other groups and ours also

emphasize the significance of polyion's electrophoretic characteristics in dictating the least charge valence of its counterpart required for coacervation: $^{31-32}$  we observed coacervation when mixing  $R_3R_4$  with the zwitterionic  $R_5D_{10}$  peptide, which can be ascribed to the pendant  $R_5$  domain on the zwitterionic backbone reinforcing electrostatic interactions (third column). These collective observations underscore the significance of balanced charge valence in regulating complex coacervation.

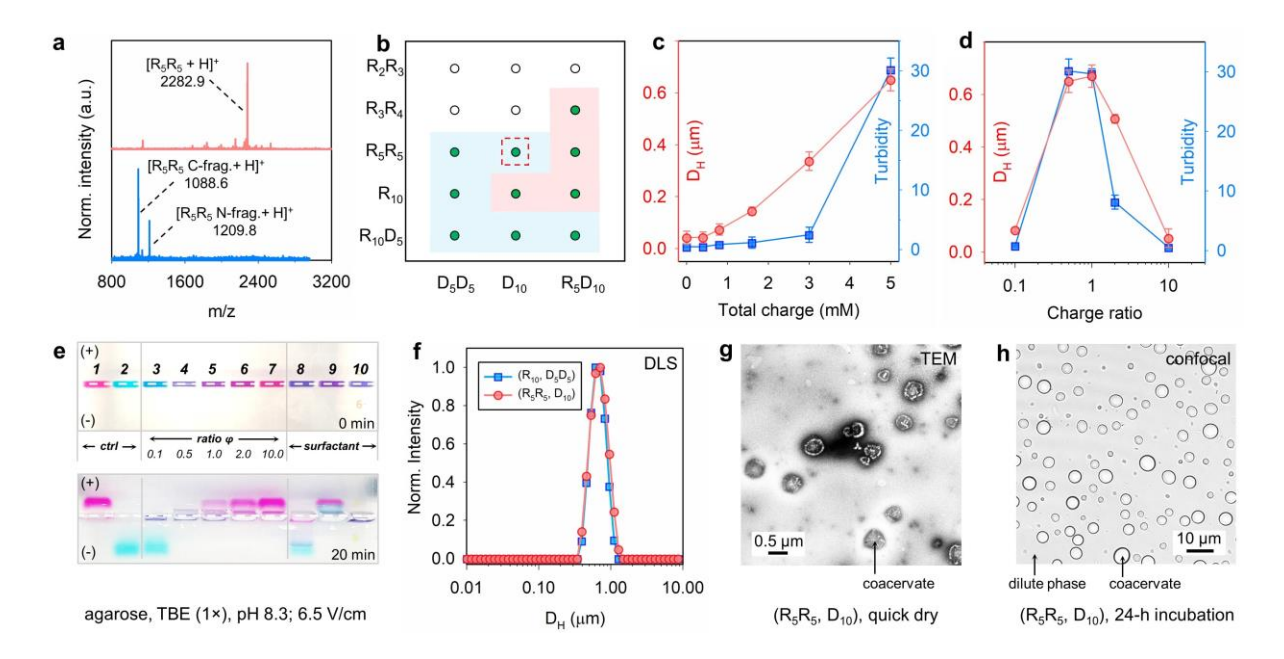


**Figure 2.** Optimization of oligopeptide coacervation. (a) MALDI-TOF MS data show that M<sup>pro</sup> cleaves the  $R_5R_5$  substrate. (b) Modular peptides of varying charge valence, charge density, and net charge are investigated for complex coacervation. The empty and green dots indicate no formation and formation of coacervates, respectively. The blue and pink shadow designates relatively stable and unstable coacervates, respectively. (c) Increasing total charge increases the hydrodynamic diameter (D<sub>H</sub>) and turbidity of freshly mixed coacervates. (d) The relation between the charge ratio (i.e., [Arg] / [Asp]) and D<sub>H</sub>/turbidity of freshly mixed coacervates. (e) Agarose gel electrophoresis acquired from the fluorogenic (Cy3-R<sub>5</sub>R<sub>5</sub>, Cy5.5-D<sub>10</sub>) coacervates of varying charge ratios (wells 3 to 7), side-by-side with the controls (Cy3-R<sub>5</sub>R<sub>5</sub> and Cy5.5-D<sub>10</sub> only in wells 1 to 2) and the coacervates with 0.2% surfactant (SDS, CTAB, and Tween-20 in wells 8 to 10). The optimal charge stoichiometry is 0.5 in well 4.<sup>33</sup> (f) DLS profiles of sub-micron coacervates by freshly mixing R<sub>5</sub>R<sub>5</sub> with D<sub>10</sub> (red) or R<sub>10</sub> with D<sub>5</sub>D<sub>5</sub> (blue). (g) TEM image of the negative-stained coacervates. (h) Bright field confocal image of the aged coacervates. The size is  $3.0 \pm 1.1$  μm. Error bars = standard deviations (n = 3).

Following that, we examined how the peptide's *net charge* influences coacervation dynamics. The net charge of -5 carried by the zwitterionic  $R_5D_{10}$  peptide exhibited coacervation properties similar to those of  $D_{10}$  (see second vs third column, **Figure 2b**). Likewise, numerous droplets were resulted by mixing the zwitterionic  $R_{10}D_5$  with either  $D_{10}$  or  $D_5D_5$  peptide. Additionally, we disclose that the zwitterionic  $R_{10}D_{10}$ , possessing a neutral net charge, undergoes self-coacervation, leading to the formation of surface wrinkles on the droplets. Therefore, the effect of net charge is marginal on the formation of coacervates.

In contrast, the *net charge* plays an important role on the colloidal stability of coacervates.<sup>34</sup> This is indicated by the zeta potential ( $\zeta$ ) and hydrodynamic diameter ( $D_H$ ) values in **Table 2**. For example, the combination of ( $R_{10}D_5$ ,  $D_{10}$ ) yielded the most stable droplets with a low surface potential of -10.4  $\pm$  1.1 mV and a compact size of  $D_H$  = 0.25  $\mu$ m. This low potential is from the negatively charged  $D_5$  moiety on  $R_{10}D_5$ . In addition,  $\zeta_{(RSR5,\,D10)}$  and  $\zeta_{(R10,\,D5D5)}$  at -6 to -7 mV showed moderate stabilities with larger sizes ( $D_H$  = 0.65  $\mu$ m). While the positively charged  $R_5$  moiety in  $R_5D_{10}$  peptide neutralized and reversed the zeta potential and led to unstable and larger droplets when mixing with  $R_{10}$ . This emphasizes the significance of adjusting the net charge of constituent peptides to improve colloidal stability and

compactness. These results coincide with recent research underscoring the role of surface electrostatics and viscosity in determining the stability of condensates.<sup>34</sup>

To this end, we have investigated the influence of *charge density* on complex coacervation, defined as the charge valence per unit length.<sup>31, 35</sup> In the first, despite  $R_5$  and  $R_{10}$  have similar charge densities, coacervation was only observed in  $(R_{10}, D_{10})$  mixture and not with  $(R_5, D_{10})$  under the same conditions. In the second,  $R_5R_5$  peptide coacervated with  $D_{10}$  despite being almost twice longer than  $R_{10}$  with a same charge valence (third row in **Figure 2a**). We found similar coacervation abilities of  $D_{10}$  and  $D_5D_5$  (first vs second column, **Figure 2a**). These observations, coupled with the existing literature, <sup>35</sup> suggest that charge density may not be crucial for coacervation.

Table 2. Hydrodynamic size (D<sub>H</sub>), polydispersity index (PDI), and surface potential of the peptide coacevates.

Peptides	D <sub>H</sub> (μm)	PDI	Zeta potential (mV)
$(R_2R_3, D_{10})$	N.D. <sup>[a]</sup>	N.D.	N.D.
(R <sub>3</sub> R <sub>4</sub> , D <sub>10</sub> )	N.D.	N.D.	N.D.
$(R_5R_5, D_{10})$	0.64	0.10	$-6.2 \pm 0.8$
$(R_{10}, D_5D_5)$	0.68	0.02	-7.4 ± 1.7
(R <sub>10</sub> D <sub>5</sub> , D <sub>10</sub> ) [b]	0.25	0.01	-10.4 ± 1.1
(R <sub>10</sub> , R <sub>5</sub> D <sub>10</sub> ) [b]	1.30	0.05	$+4.4 \pm 0.5$
$(R_{10}D_{10})^{[b]}$	1.78	0.05	$+5.7 \pm 0.3$

[a] 'N.D.' designates coacervate Not Detected by DLS. The conditions used 5 mM total charge, 0.5 charge ratio, 20 mM PB at pH 8, and 0.2% Tween-20 unless otherwise specified. [b] For zwitterionic peptides, the charge ratio uses [Arg, (+)] = [net-positively-charged peptide]  $\times$  Arg valence, and [Asp, (-)] = [net-negatively-charged peptide]  $\times$  Asp valence. *Remark:* the charge ratio in  $D_{10}R_{10}$  self-coacervates is 1.

### 2.3 Coacervate characterization

We exploited a representative ( $R_5R_5$ ,  $D_{10}$ ) system and optimized the conditions such as total charge (from peptides, [Arg] + [Asp]), charge ratio ([Arg] / [Asp]), pH, ionic strength (from inorganic salts), and surfactants. In **Figure 2c**, we observed a slight increase in turbidity at *total charges* of 0.8 - 3 mM, followed by a substantial rise when exceeding 3 mM. This indicates the formation of numerous droplets. The corresponding DLS measurement showed a similar trend, with a critical total charge of 0.8 mM resulting in a droplet size of 0.1  $\mu$ m. We chose 5 mM total charge for subsequent experiments, which gave a sufficient number of droplets.

Next, a closer examination in gel electrophoresis demonstrated that the optimal charge stoichiometry is 0.5 for (Cy3-R<sub>5</sub>R<sub>5</sub>, Cy5.5-D<sub>10</sub>) system using the dye-labeled peptides, with approximately 100% of the peptides concentrated in coacervates (**Figure 2d,e**). Different charge ratios and control samples included free peptide-dye migrating towards either the cathode or anode. The lack of mobility shift observed for the coacervates at 0.5 charge ratio was due to their large size compared to the dimensions of the pores (see well 4, **Figure 2e**), <sup>33</sup> rather than a charge neutrality.

The *size* of coacervates was then characterized by DLS, TEM, and confocal microscope. The fresh coacervates showed a  $D_H$  of 0.64  $\mu m$  with a low polydispersity index PDI = 0.09, indicative of a homogeneous population of droplets (**Figure 2f**). Other peptide combinations, such as ( $R_{10}$ ,  $D_5D_5$ ), also exhibited coacervates in the (sub)micrometer regime with an average size of 0.68  $\mu m$  (**Table 2**). TEM images outlined sub-populations of stained coacervates with a size range of 0.4 to 0.8  $\mu m$  (**Figure 2g**). Confocal microscopy posed challenges due to the rapid movement of droplets. However, after allowing the samples to age, the majority of coacervates settled, enabling imaging with an average size of 3.0  $\pm$  1.1  $\mu m$  (**Figure 2h**). The observed droplet enlargement after aging can be attributed to coalescence facilitated by the fluid-like character of the membrane-less system.<sup>20, 36</sup>

To enhance colloidal stability and reduce interparticle coalescence, we incorporated the non-ionic *surfactant* Tween-20 (0.2% w/v) during the coacervation of  $(R_5R_5, D_{10})$  peptides.<sup>37</sup> The efficacy of this approach was monitored by time-resolved turbidity measurements, as shown in **Figure 3a**. Tween-20 significantly slowed turbidity decay compared to the surfactant-free control, preserving 70% of initial turbidity after 3 h. In contrast, the control experienced an 80% turbidity drop within 0.5 h, and microscopy revealed a bulk liquid instead of well-dispersed droplets. This discrepancy is attributed to the Tween-20 above critical micelle concentration (CMC) acts as non-interacting physical barrier and impedes colliding coalescence of the membrane-less droplets. Gel electrophoresis confirmed that Tween-20 did not compromise the droplet integrity (see well 10, **Figure 2e**). In contrast, ionic surfactants such as SDS and CTAB, above their CMC, disrupted our complex coacervates by engaging in electrostatic competition with the counter polyions (wells 8-9).<sup>29,38</sup> This further verifies that electrostatic interactions are the predominant driving force in our system. Collectively, Tween-20 emerges as a straightforward method for stabilizing non-membrane coacervates.<sup>20,36</sup>

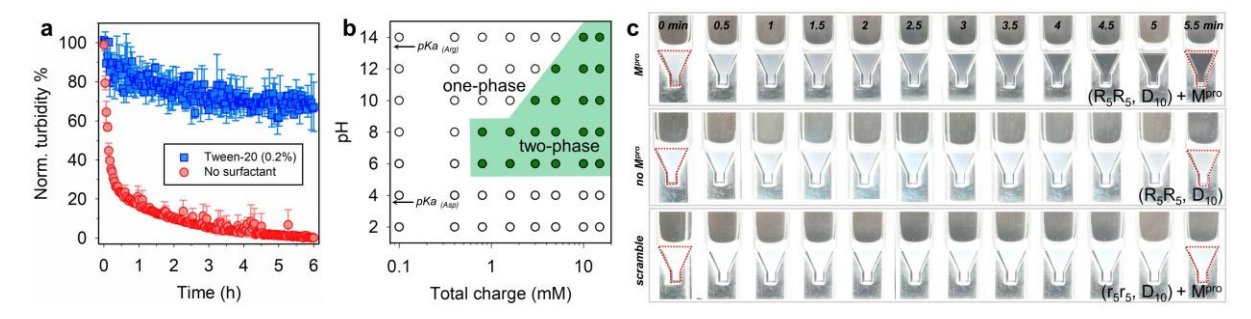


**Figure 3.** (a) The turbidity decay of the ( $R_5R_5$ ,  $D_{10}$ ) coacervates with (blue) and without (red) 0.2% w/v Tween-20. (b) Phase diagram indicates that pH 6 - 8 is the optimal pH range for ( $R_5R_5$ ,  $D_{10}$ ) coacervation. The green area designates coacervation. (c) Time-dependent turbidity decay of the ( $R_5R_5$ ,  $D_{10}$ ) coacervates with  $M^{pro}$ . [S]: [E] = 800:1 was applied. Controls used without  $M^{pro}$  and a scramble  $r_5r_5$  peptide with  $M^{pro}$ . Error bars = standard deviations (n = 3).

pH and ionic strength are crucial factors that determine the outcome of coacervation. In **Figure 3b**, a pH range of 6 - 14 is essential for the coacervation of (R<sub>5</sub>R<sub>5</sub>, D<sub>10</sub>) peptides because deprotonation of the carboxyl in Asp occurs above  $pK_a \approx 3.9$ . However, overly basic conditions hinder coacervation, likely due to the deprotonation of guanidinium group in Arg ( $pK_a \approx 13.8$ )<sup>40</sup> and high ionic strength. Therefore, the optimal pH range for favorable (R<sub>5</sub>R<sub>5</sub>, D<sub>10</sub>) coacervation is near the physiological range.<sup>23</sup>

Regarding ionic strength, it is widely recognized that low ionic strength promotes complex coacervation, as illustrated by our observed empirical correlation between the maximum NaCl concentration and the total charge of coacervates:  $[NaCl]_{max} \approx [total\ charge] \times 10$ . The salt stability of  $(R_5R_5,\ D_{10})$  coacervates is specific to NaCl because sub-millimolar concentrations of  $CaCl_2$  rapidly crosslinks and aggregates the droplets.<sup>30, 41</sup> In summary, we optimized a phosphate buffer (20 mM, pH 8.0) without NaCl but with 0.2% (w/v) Tween-20 to investigate the interactions between the coacervates and  $M^{pro}$ .

# 2.4 Enzyme modeling with non-fluorescent coacervates

We asked whether M<sup>pro</sup> interacts with R<sub>5</sub>R<sub>5</sub> substrate trapped within the (R<sub>5</sub>R<sub>5</sub>, D<sub>10</sub>) coacervates. To generate coacervate samples, the peptides were mixed thoroughly in a clear cuvette for 10 s, and the resulting turbid dispersion was photographed every 30 s. Other conditions used 5 mM total charge, 0.5 charge ratio, 20 mM PB (pH 8), 0.2% Tween-20,

and a substrate-to-enzyme ratio of 800:1. In **Figure 3c**, the addition of 200 nM  $M^{pro}$  to the opaque emulsion led to a clear solution in 5.5 min. This offered compelling proof of the protease cleaving the confined  $R_5R_5$  substrate, generating fragments unable to maintain the required charge valency essential for sustained coacervation. The control trial without  $M^{pro}$  remained turbid. The coacervates constituting the scramble sequence  $r_5r_5$  and  $M^{pro}$  also showed no turbidity drop, indicating the need for specific recognition between substrate and protease.

# 2.5 Enzyme modeling with self-quenching coacervates

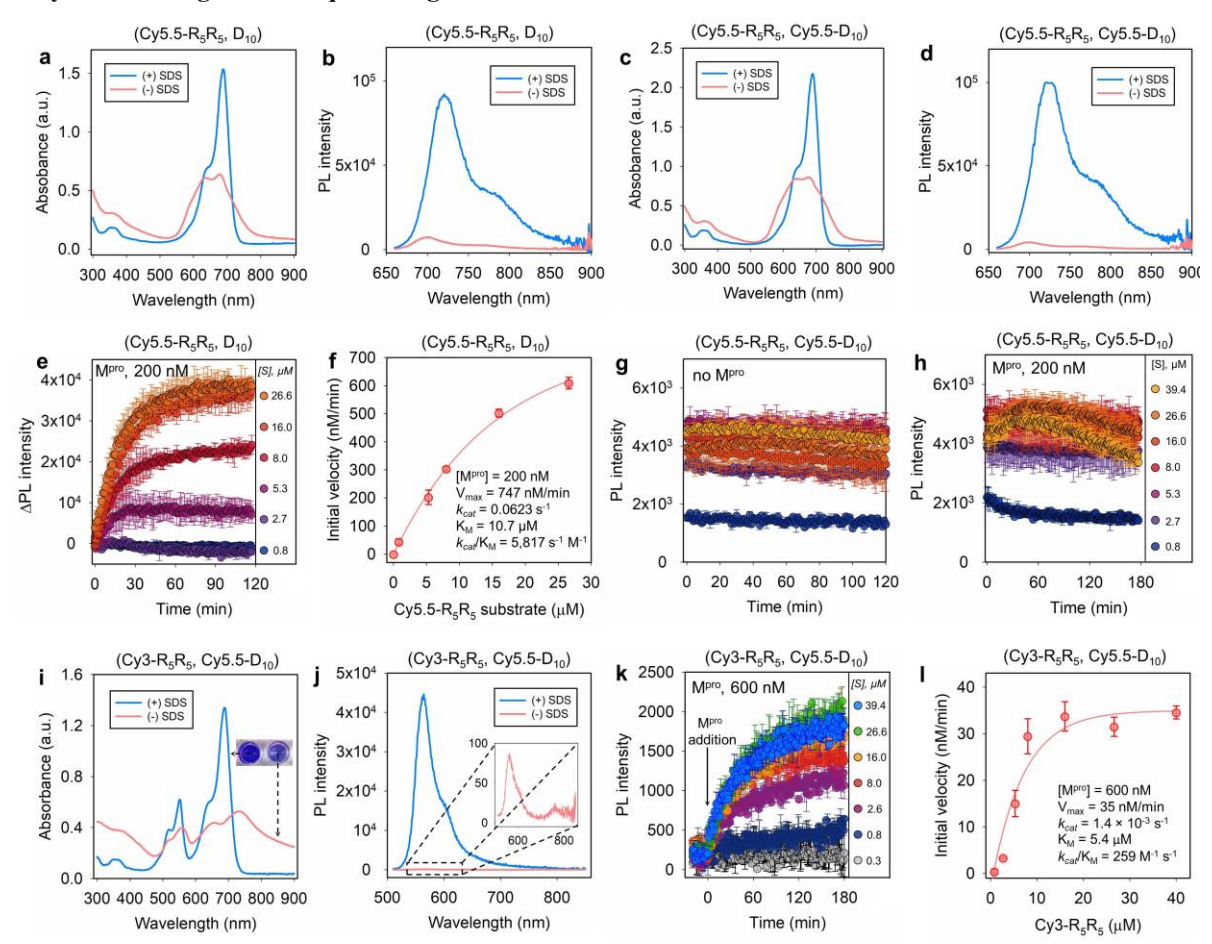


**Figure 4.** Enzyme studies of fluorogenic coacervates. Absorption (**a,c**) and PL (**b,d**) of the (Cy5.5-R<sub>5</sub>R<sub>5</sub>, D<sub>10</sub>) and (Cy5.5-R<sub>5</sub>R<sub>5</sub>, Cy5.5-D<sub>10</sub>) coacervates with (blue) and without (red) 1% SDS, respectively. (**e**) Time-dependent  $\Delta$ PL<sub>720 nm</sub> of the coacervates at various total charges (0.024 – 0.8 mM) incubated with M<sup>pro</sup> (200 nM). This corresponds to final [S] concentrations of 0.8 – 26.6 μM. (**f**) Determination of  $k_{cat}/K_M = 5,817$  M<sup>-1</sup> s<sup>-1</sup> for hydrolysis of the (Cy5.5-R<sub>5</sub>R<sub>5</sub>, D<sub>10</sub>) coacervates by M<sup>pro</sup> in 20 mM PB, pH 8.0, at 37 °C. Time-dependent PL<sub>720 nm</sub> of the (Cy5.5-R<sub>5</sub>R<sub>5</sub>, Cy5.5-D<sub>10</sub>) coacervates of various total charge (0.024 – 1.2 mM) without (**g**) and with (**h**) M<sup>pro</sup> (200 nM) over 3 h. This corresponds to a final [S] concentration of 0.8 – 39.4 μM. Absorption (**i**) and fluorescence (**j**) profile of the FRET-based (Cy3-R<sub>5</sub>R<sub>5</sub>, Cy5.5-D<sub>10</sub>) coacervates with (blue) and without (red) 1% SDS. The inset picture shows a slight color change upon coacervation. (**k**) Time-dependent PL<sub>560 nm</sub> recovery of the FRET coacervates at varying total charges from 0.024 mM to 1.2 mM incubated with M<sup>pro</sup> (600 nM). This corresponds to final Cy3-R<sub>5</sub>R<sub>5</sub> concentrations from 0.8 μM to 39.4 μM. (**l**) Determination of  $k_{cat}/K_M$  for hydrolysis of the FRET coacervates by M<sup>pro</sup>.

Coacervates demonstrate a confined structure and facilitate energy transfer-based transductions by bringing interacting moieties close together. Other research groups have utilized this feature to investigate associations both within and between coacervates. However, the subsequent dissolution of coacervates has received little attention, which also impacts the separation distance and energy transfer. Here, we used a dye-labeled peptide in the  $(Cy5.5-R_5R_5, D_{10})$  and  $(Cy5.5-R_5R_5, Cy5.5-D_{10})$  coacervates and realized a self-quenching 43-44 effect resulting from an increase in the local dye

concentration, reaching approximately 100-fold based on related work.<sup>4, 19, 45</sup> We also observed that integration of Cy5.5 dye to the coacervate led to a reduction in the critical total charge from 0.8 mM for ( $R_5R_5$ ,  $D_{10}$ ) to 0.024 mM. This is presumably due to additional cation- $\pi$  interactions that reinforce the interpeptide association. Following the addition of  $M^{pro}$ , the coacervates were disassembled, the dye PL was recovered, and this enabled the modeling of enzyme kinetics.

**Figure 4a-d** shows the immediate optical differences of conjugated Cy5.5 upon incorporation into coacervated. The introduction of 1% w/v SDS (above CMC) to coacervates is twofold: (i) it breaks the ion-pairing interactions and disassembles the coacervates, <sup>29</sup> and (ii) it minimizes dye-dye stacking interactions and favors its monomeric state. <sup>38, 46</sup> The absorbance peak wavelength ( $\lambda_{max}$ ) of Cy5.5 in coacervates blue-shifts from 687 nm for the monomeric dye to 677 nm, indicating strong intermolecular interactions of Cy5.5.<sup>44</sup> This shift is accompanied by intensity reductions of the hypochromic peak and peak broadening. The PL peak wavelength also exhibits a 20-nm hypochromic shift along with a high PL quenching efficiency of 93%. This efficiency is calculated using  $E\% = 1 - PL_{coacervate}/PL_{free}$ . The decrease in quantum yields from 0.16 for the free dye to 0.05 also supports the observed PL quenching. Our group has reported near-complete self-quenching of the dye PL, realized by bringing a dye dimer in close proximity using a short linker. <sup>44</sup>

Next, we monitored the reaction of  $M^{pro}$  (200 nM) on the fluorogenic coacervates with varying total charges ranging from 0.024 mM to 0.8 mM. The  $\Delta PL$  at 720 nm ( $PL_t - PL_\theta$ ) was recorded for 2 h at 37 °C and pH 8. By modulating the total charges, we could simultaneously adjust the substrate concentrations ranging from 0.8  $\mu$ M to 26.6  $\mu$ M. **Figure 4e** shows that the enhancement in the  $\Delta PL_{720 \text{ nm}}$  with time that is commensurate with the Cy5.5-R<sub>5</sub>R<sub>5</sub> employed. Up to 2.7-fold PL recovery was measured at a substrate concentration of 16  $\mu$ M. The control showed no PL enhancement under identical conditions in the absence of  $M^{pro}$ . Therefore, we selected a substrate concentration of 16  $\mu$ M for further study unless otherwise indicated.

The progressive increase in PL demonstrates that the digestion of the (Cy5.5-R<sub>5</sub>R<sub>5</sub>, D<sub>10</sub>) coacervates releases the dye from the droplets. The data in **Figure 4e** were further converted to the amount of cleaved Cy5.5-R<sub>5</sub>R<sub>5</sub> for quantifying the kinetic parameters. To do this, we retrieved the proteolyzed samples at 12 h and quantified the dye amount in the supernatant (i.e., fragment). A linear standard curve was found between the  $\Delta$ PL and the dye-fragment concentration. This linear fit was then used to back-calculate the amount of product in the real-time proteolysis and build a classical Michaelis-Menten (MM) plot. Our results show that M<sup>pro</sup> can digest up to 75% of the coacervates, while the portion remaining undigested can be attributed to the bulk phase induced by coalescence and sedimentation, rendering the substrate inaccessible to the protease. (**Table 3**).

Transduction mechanism	Component	M <sup>pro</sup> , nM	v <sub>max</sub> , nM/min	kcat, s-1	<b>К</b> м, μ <b>М</b>	k <sub>cat</sub> /K <sub>M</sub> , M <sup>-1</sup> s <sup>-1</sup>	Digestion yield <sup>[b]</sup>
FRET probe	Cy5.5-R <sub>5</sub> R <sub>5</sub> C-Cy3	200	780	0.065	12.6	5,159	85%
Self-quenching	$(Cy5.5-R_5R_5, D_{10})$	200	747	0.062	10.7	5,817	75%
coacervate	(Cy5.5-R <sub>5</sub> R <sub>5</sub> , Cy5.5- D <sub>10</sub> )	200	N.D. [a]	N.D.	N.D.	N.D.	0%
FRET coacervate	(Cy3-R <sub>5</sub> R <sub>5</sub> , Cy5.5-D <sub>10</sub> )	600	35	0.0014	5.4	259	5%

[a] 'N.D.' designates Not Determined. [b] The yield for FRET probe is from area integration in HPLC, and that for coacervates is estimated from the absorbance of the supernatant using  $\epsilon_{Cy3} = 1.5 \times 10^5 \text{ M}^{-1} \text{ cm}^{-1}$  at Abs<sub>555 nm</sub> and  $\epsilon_{Cy5.5} = 1.98 \times 10^5 \text{ M}^{-1} \text{ cm}^{-1}$  at Abs<sub>685 nm</sub>.

The specificity constant,  $k_{cat}/K_M$ , for the (Cy5.5-R<sub>5</sub>R<sub>5</sub>, D<sub>10</sub>) coacervates by M<sup>pro</sup> was calculated to be 5,817 M<sup>-1</sup> s<sup>-1</sup> (**Figure 4f**). This finding provides valuable insights into the interactions between non-membrane droplets and enzymes, as a comparison of  $k_{cat}/K_M$  for the substrate in coacervate versus in solution has not been previously reported. To address this, we further measured the  $k_{cat}/K_M$  for free substrate by M<sup>pro</sup> using a synthetic peptide (Cy5.5-R<sub>5</sub>R<sub>5</sub>C-Cy3) and obtained a value of 5,159 M<sup>-1</sup> s<sup>-1</sup>. This value is slightly or 1.1-fold lower than that of coacervates. In this case, both systems exhibited a similar  $K_M$  value of 10  $\mu$ M, which indicates that M<sup>pro</sup> binds to the substrate with a comparable

affinity irrespective of the coacervates.<sup>47</sup> The obtained specificity constants are consistent with prior findings.<sup>41, 48</sup> The slight differences may arise from variations in assay conditions or substrate sequence customization (**Table 3**).

We then examined the kinetics of M<sup>pro</sup> on (Cy5.5-R<sub>5</sub>R<sub>5</sub>, Cy5.5-D<sub>10</sub>) coacervates and compared to that of the previous (Cy5.5-R<sub>5</sub>R<sub>5</sub>, D<sub>10</sub>) droplets. Self-quenching in optical profiles of (Cy5.5-R<sub>5</sub>R<sub>5</sub>, Cy5.5-D<sub>10</sub>) were observed (**Figure 4c.d**). However, the introduction of M<sup>pro</sup> to the (Cy5.5-R<sub>5</sub>R<sub>5</sub>, Cy5.5-D<sub>10</sub>) samples showed no PL recovery, with the intensity remaining a constant for over 3 h (Figure 4g,h). The control without M<sup>pro</sup> yielded the same result. To confirm the effect of hydrophobicity effect on the enzyme-coacervate interactions, we further measured the kinetics on fluorescence resonance energy transfer (FRET)-based (Cy3-R<sub>5</sub>R<sub>5</sub>, Cy5.5-D<sub>10</sub>) coacervates. The PL profile exhibited a substantial donor quenching with an efficiency more than 99.9 % (Figure 4i,j). We monitored the PL<sub>560 nm</sub> for M<sup>pro</sup> (600 nM) interacting with the (Cy3-R<sub>5</sub>R<sub>5</sub>, Cy5.5-D<sub>10</sub>) coacervates at various total charges (0.024 – 1.2 mM). Figure 4k shows that more PL recovery of Cy3 donor is observed for higher substrate concentration, implying that M<sup>pro</sup> releases partial of the coupled Cy3 from the droplets. However, the attainment of kinetic equilibrium required an hour-scale time and resulted in a low digestion yield of 5% (Table 3). In Figure 4I, the (Cy3-R<sub>5</sub>R<sub>5</sub>, Cy5.5-D<sub>10</sub>) coacervates with M<sup>pro</sup> exhibited a k<sub>cat</sub>/K<sub>M</sub> of 259 M<sup>-1</sup> s<sup>-1</sup>, which was about 20-fold lower than that of the free substrate (**Table 3**).<sup>41, 48</sup> The decrease in specificity constant was primarily attributed to a decrease in turnover number  $(k_{cat})$ , while  $K_M$  remained at a similar level (5-15 μM). This behavior resembles to non-competitive inhibition, where the inhibitor binds to a non-active site of the enzyme. We thus suggest that the inclusion of larger hydrophobic moieties in (R<sub>5</sub>R<sub>5</sub>, D<sub>10</sub>) coacervates is likely to bind to the hydrophobic domain of M<sup>pro</sup>, distinct from the active site, resulting in a reduction in enzyme kinetics. This observation is consistent with a previous study by Gianneschi et al., where an increase in the hydrophobicity of the scaffold leads to a decrease in the associated peptide cleavage sites due to limited water solvent molecules, thereby reducing their accessibility to proteolytic enzymes.

Our results are not uncommon, as the study of enzyme kinetics on various scaffolds such as polymers, particles, or membranes has been a subject of discussion, with some supporting a slow kinetic model that considers slow diffusion, increased hydrophobicity, and steric crowdedness, <sup>49-51</sup> while others favor a fast kinetic model that emphasizes enzyme hopping and high local concentration. <sup>52</sup> On the one hand, our finding on (Cy5.5-R<sub>5</sub>R<sub>5</sub>, D<sub>10</sub>) coacervates agrees with a recent study by Keating *et al.*, showing that phosphatase exhibits slightly higher activity towards substrates within coacervates compared to free substrates, and kinase activity was not significantly altered by the presence of coacervates. <sup>9</sup> On the other hand, we stress that the bioactivity of coacervates for proteolysis can be fine-tuned by changing the scaffold properties such as hydrophobicity and others.

# 2.6 Inhibition, specificity, and matrix effects

The identification of a characteristic specificity constant with  $M^{pro}$  in responsive (Cy5.5-R<sub>5</sub>R<sub>5</sub>, D<sub>10</sub>) coacervates signifies a promising platform for enzyme studies. To estimate the limit of detection (LoD), increasing amount of  $M^{pro}$  from 0 – 500 nM were incubated with (Cy5.5-R<sub>5</sub>R<sub>5</sub>, D<sub>10</sub>) coacervates containing a fixed amount of substrate at 16  $\mu$ M. **Figure 5a** indicates that higher  $M^{pro}$  concentration resulted in more PL recovery, and *vice versa*. **Figure 5b** shows the  $\Delta PL_{720 \text{ nm}}$  as a function of  $M^{pro}$  concentration at 1 h readout time: The LoD was determined to be 55.7 nM, following a previously established method.<sup>53</sup> This LoD is 2-fold higher than that of our previous colorimetric sensors due to the short readout time of the current system.<sup>29</sup>

The confirmed PL recovery resulting from targeted proteolysis was validated through inhibition assays. For example,  $M^{pro}$  (200 nM) was incubated with GC376 inhibitor at varying molar ratios ([I]/[E] = 0 - 10) for 10 min before mixing with (Cy5.5-R<sub>5</sub>R<sub>5</sub>, D<sub>10</sub>) coacervates containing 16  $\mu$ M substrate. In **Figure 5c**, increased inhibitor concentrations led to reduced enzymatic reactions and delayed PL recovery, with a tenfold excess of GC376 inhibiting protease activity. This excludes the PL recovery by non-specific interactions between the coacervates and M<sup>pro</sup>. A closer examination of the PL<sub>720 nm</sub> at 30 min yields a typical inhibitor titration curve (**Figure 5d**). The Henderson equation estimated the active M<sup>pro</sup> fraction to be 70%, and the potency of GC376 inhibitor is  $K_{i \text{ (app)}} = 138 \text{ nM}$  and  $IC_{50} = 208 \text{ nM}$ . These values are in line with our previous findings. The specificity of (Cy5.5-R<sub>5</sub>R<sub>5</sub>, D<sub>10</sub>) coacervates was evaluated towards other proteins (200 nM), including trypsin, thrombin,  $\alpha$ -amylase (200 U/mL<sup>57</sup>), bovine serum albumin (BSA), and hemoglobin. In **Figure 5e**, no PL activation was detected in the presence of BSA, hemoglobin, and other enzymes, except for trypsin, which led to an undesired signal higher than that of M<sup>pro</sup>. This comes as no surprise, considering that trypsin cleaves at the C-terminal of Arg, and the R<sub>5</sub>R<sub>5</sub> substrate includes multiple potential cleavage sites. <sup>29, 47</sup>

We evaluated matrix effects by spiking the (Cy5.5-R<sub>5</sub>R<sub>5</sub>, D<sub>10</sub>) coacervates in PB buffer, exhaled breath condensate (EBC),<sup>29</sup> urine, DMEM culture media, BSA solution (1% w/v), human pooled saliva,<sup>57</sup> and human plasma.<sup>58</sup> We first

assessed the stability of (Cy5.5-R<sub>5</sub>R<sub>5</sub>, D<sub>10</sub>) coacervates in the above matrices. The coacervates showed great stability without PL changes in buffer, EBC, urine, and saliva. Nonetheless, these coacervates showed rapid dissolution in high concentrations of BSA and were prone to competitive binding with constituents in cell growth media and human plasma, thus leading to fully recovered PL prior to the onset of proteolysis.<sup>59</sup> Subsequently, 200 nM of  $M^{pro}$  was introduced to the coacervates in buffer, EBC, urine, and saliva, and the time-dependent PL recovery was recorded. **Figure 5f** shows the relative PL changes at 20 min in various matrices by establishing a complete PL recovery in buffer as the topline. The interactions between coacervates and the enzyme remained consistent in buffer, EBC, and urine. The coacervates in saliva showed a 19% PL recovery independent of  $M^{pro}$  addition, presumably due to non-specific interactions.<sup>60</sup>

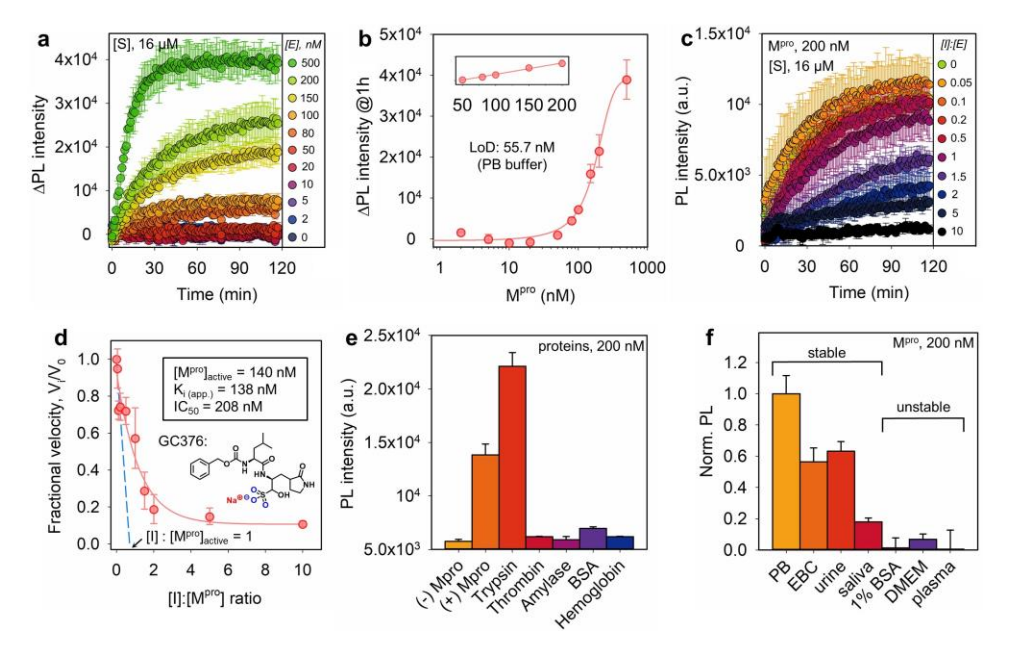


**Figure 5.** Enzyme studies of the self-quenching-based (Cy5.5-R<sub>5</sub>R<sub>5</sub>, D<sub>10</sub>) coacervates. (a) Time progression of  $\Delta PL_{720 \text{ nm}}$  in enzyme sensitivity assays, where the coacervates at 0.48 mM total charge ([S] = 16 μM) were incubated with increasing M<sup>pro</sup> concentrations from 0–500 nM. (b) The PL<sub>720 nm</sub> as a function of M<sup>pro</sup> concentration was extracted from panel (a) at 1 h. The limit of detection (LoD) is 55.7 nM in PB buffer. The inset shows the linear fit for LoD calculation.<sup>53</sup> (c) Time-dependent PL<sub>720 nm</sub> in inhibition assays. Increasing molar ratio of [I]/[E] from 0 – 10 was employed where GC376 is used as the inhibitor. (d) Inhibition curve collected by titrating M<sup>pro</sup> (200 nM) with varying amounts of GC376; the coacervates at 0.48 mM total charge were used. The inset shows the chemical structure of GC376 inhibitor. (e) The reactivity of the fluorogenic coacervates towards other proteins (200 nM).<sup>57</sup> (f) The interactions of the fluorogenic coacervates with M<sup>pro</sup> in biological matrices. All the above time progression data were collected every 1 min for 2 h, and the ΔPL<sub>720 nm</sub> = PL<sub>t</sub> - PL<sub>θ</sub> was used for the plot. Error bars = standard deviations (n = 3).

# 3. CONCLUSION

We have studied the interactions between complex coacervates and main protease. The non-membrane coacervates constitute of  $R_3R_5$  and  $D_{10}$ . We first identified several optimal conditions for coacervation: (i) The lowest charge valence for Arg-peptide was 10, given  $D_{10}$  as the counter polyanion. (ii) The critical total charge was 0.8 mM. (iii) The exact charge ratio was 0.5 for a 100% of peptide complexation. (iv) pH above 6 was required. (v) A 0.2% non-ionic Tween-20 enhanced the stability. We found that the enzyme-coacervate interactions depend on the specific nature of the droplets, such as the quantity of dye integrated. The incorporation of one dye-labeled strand has a minimal effect on the interacting kinetics [e.g.,  $k_{cat}/K_{\rm M} = 5,817~{\rm M}^{-1}~{\rm s}^{-1}$  for (Cy5.5-R<sub>5</sub>R<sub>5</sub>, D<sub>10</sub>) coacervates], while two dye-labeled strands [e.g., (Cy5.5-R<sub>5</sub>R<sub>5</sub>, Cy5.5-D<sub>10</sub>) coacervates] essentially quench the proteolysis reactions. This work presents a simple design of enzyme-responsive coacervates and provides informative insights into the tunable interactions between the enzyme and complex coacervates as a substrate hub.

#### 4. EXPERIMENTAL SECTION

#### 4.1 Materials

Fmoc-protected amino acids, hexafluorophosphate benzotriazole tetramethyl uronium (HBTU), and Fmoc-Rink amide MBHA resin (0.67 mmol/g, 100-150 mesh) were purchased from AAPPTec, LLC (Louisville, KY). The recombinant SARS-CoV-2 main protease (M<sup>pro</sup>) was expressed using the M<sup>pro</sup> plasmid provided by Prof. Rolf Hilgenfeld, University of Lübeck, Germany and purified as previously described.<sup>48</sup> The N-hydroxysuccinimide (NHS)-ester dyes were from Lumiprobe Corp. (Hunt Valley, MD). Ultrapure water (18 MΩ.cm) was obtained from a Milli-Q Academic water purification system (Millipore Corp., Billerica, MA). More materials can be found in SI.

## 4.2 Peptide synthesis

Peptides were chain assembled by Fmoc-SPPS (solid-phase peptide synthesis) on Rink-amide-MBHA-resin (0.67 mmol/g, 200 mg) following our previous protocol using an automated Eclipse<sup>TM</sup> peptide synthesizer (AAPPTec, Louisville, KY).<sup>41</sup> The synthetic peptides were cleaved from the resin using the cleavage cocktail (3 mL) that contained TFA (82.5%), EDDET (2.5%), phenol (5%), thioanisole (5%), and H<sub>2</sub>O (5%). Resins were treated with the cleavage cocktail for 10-12 h with gentle shaking to ensure a full cleavage of side chain protection groups. The peptides were purified by the reversed phase HPLC (Shimadzu LC-40), confirmed by the MALDI-TOF MS, aliquoted ( $\epsilon_{205} = 31 \, \text{mL·mg}^{-1} \cdot \text{cm}^{-1}$ ) using a NanoDrop<sup>TM</sup> One UV-vis spectrophotometer (Thermo Fisher Scientific), and stored in dry conditions at room temperature for further use.

## 4.3 Cy5.5-labeled peptides

An aqueous solution of  $D_{10}$  peptide (3.0 mg or 2.6  $\mu$ moles, in 1 mL of PB, pH 8.0) was mixed with NHS-Cy5.5 (1.0 mg or 1.3  $\mu$ moles, in 1.5 mL of DMSO); the final pH of the mixture was adjusted to ~8 using NaOH solution (1 M) if needed. The reaction was stirred for 1 h protected from light, followed by drying in a speed vacuum system at 60 °C. The conjugation yield was ~40% after HPLC purification.

# 4.4 Coacervates preparation

The complex coacervates (60  $\mu$ L) were prepared by thoroughly mixing the desired amount of negatively charged peptides, PB buffer (20 mM, pH 8.0), and positively charged peptides in order at room temperature. Coacervate formation was initially examined by an optical microscope (40×) on a EVOS XL Core imaging System (Thermo Fisher Scientific). The fluorogenic coacervates were typically studied at a total charge of 0.48 mM (e.g., for detection limits) and 0.8 mM (e.g., for studying photophysical properties). For example, the conditions of  $R_5R_5$ -Cy5.5 and  $D_{10}$  at 0.5 charge ratio and 0.48 mM total charge used the  $D_{10}$  (2.1 mM, 0.92  $\mu$ L), PB (20 mM, pH 8.0, 0.2% Tween-20, 54.7  $\mu$ L), and  $R_5R_5$ -Cy5.5 (0.78 mM, 1.2  $\mu$ L) in order.

# 4.5 Proteolysis on self-quenching coacervates

A series of coacervates (charge ratio = 0.5, pH 8, 0.2% Tween-20, 60  $\mu$ L) with various total charges (*i.e.*, 0.024, 0.08, 0.16, 0.24, 0.48, 0.8, and 1.2 mM) were prepared by thoroughly mixing a desirable amount of D<sub>10</sub> (2.1 mM in PB, pH 8), PB (20 mM, pH 8, 0.2% Tween-20), and R<sub>5</sub>R<sub>5</sub>-Cy5.5 (0.78 mM in PB, pH 8) in order in a 96-well plate. This corresponds to a final *substrate concentration* (here, [S]<sub>0</sub>, or [R<sub>5</sub>R<sub>5</sub>-Cy5.5]) of 0.8, 2.7, 5.3, 8.0, 16, 26.6, and 39.4  $\mu$ M. The resulted coacervates were then pre-incubated at 37 °C for 20 min using a hybrid multi-mode microplate reader to stabilize the PL signal. Next, the desired amount of M<sup>pro</sup> ([M<sup>pro</sup>]<sub>final</sub> = 200 nM, 70% active) was then added to each well, and the mixture was thoroughly pipetted. The plate was immediately sealed and incubated at 37 °C in the hybrid multi-mode microplate reader with 3 s of shaking before each cycle of reading, and the PL intensity (excitation/emission wavelength = 630 nm/720 nm) was recorded over 12 h with 1 min intervals between each cycle. Control used the same protocol without introducing M<sup>pro</sup>. Experiment was done in triplicate.

# **ACKNOWLEDGEMENTS**

The authors thank Dr. Anthony J O'Donoghue and Dr. Pavla Fajtová in the UC San Diego for kindly providing the M<sup>pro</sup>. We also thank the National Institutes of Health (R01 DE031114; R21 AG065776-S1; R21 AI157957) for financial support. We thank NSF under grant #1845683. This work was also supported by National Science Foundation (DMR-2011924) via equipment in the UC San Diego Materials Research Science and Engineering Center (UCSD MRSEC).

Proc. of SPIE Vol. 12859 1285903-11

The electron microscopy work was performed in part at the San Diego Nanotechnology Infrastructure (SDNI) of University of California San Diego, a member of the National Nanotechnology Coordinated Infrastructure (NNCI), which is supported by the National Science Foundation (Grant ECCS-1542148).

#### REFERENCES

- 1. Brangwynne, C. P.; Eckmann, C. R.; Courson, D. S.; Rybarska, A.; Hoege, C.; Gharakhani, J.; Jülicher, F.; Hyman, A. A., Germline P Granules Are Liquid Droplets That Localize by Controlled Dissolution/Condensation. Science **2009**, 324, 1729-1732.
- 2. Yang, P.; Mathieu, C.; Kolaitis, R.-M.; Zhang, P.; Messing, J.; Yurtsever, U.; Yang, Z.; Wu, J.; Li, Y.; Pan, Q.; Yu, J.; Martin, E. W.; Mittag, T.; Kim, H. J.; Taylor, J. P., G3BP1 Is a Tunable Switch that Triggers Phase Separation to Assemble Stress Granules. Cell **2020**, 181, 325-345.e28.
- 3. Xu, C.; Martin, N.; Li, M.; Mann, S., Living material assembly of bacteriogenic protocells. Nature **2022**, 609 (7929), 1029-1037.
- 4. Hughes, M. P.; Sawaya, M. R.; Boyer, D. R.; Goldschmidt, L.; Rodriguez, J. A.; Cascio, D.; Chong, L.; Gonen, T.; Eisenberg, D. S., Atomic structures of low-complexity protein segments reveal kinked beta-sheets that assemble networks. Science **2018**, 359, 698-701.
- 5. Mu, W.; Ji, Z.; Zhou, M.; Wu, J.; Lin, Y.; Qiao, Y., Membrane-confined liquid-liquid phase separation toward artificial organelles. Sci. Adv. **2021**, 7, eabf9000.
- Sun, Y.; Lau, S. Y.; Lim, Z. W.; Chang, S. C.; Ghadessy, F.; Partridge, A.; Miserez, A., Phase-separating peptides for direct cytosolic delivery and redox-activated release of macromolecular therapeutics. Nat. Chem. 2022, 14, 274-283.
- 7. Zhang, P.; Fan, B.; Yang, P.; Temirov, J.; Messing, J.; Kim, H. J.; Taylor, J. P., Chronic optogenetic induction of stress granules is cytotoxic and reveals the evolution of ALS-FTD pathology. eLife **2019**, 8, e39578.
- 8. Kubota, R.; Torigoe, S.; Hamachi, I., Temporal Stimulus Patterns Drive Differentiation of a Synthetic Dipeptide-Based Coacervate. J. Am. Chem. Soc. **2022**, 144, 15155-15164.
- 9. Aumiller, W. M.; Keating, C. D., Phosphorylation-mediated RNA/peptide complex coacervation as a model for intracellular liquid organelles. Nature Chem. **2016**, 8, 129-137.
- 10. Gibson, B. A.; Doolittle, L. K.; Schneider, M. W. G.; Jensen, L. E.; Gamarra, N.; Henry, L.; Gerlich, D. W.; Redding, S.; Rosen, M. K., Organization of Chromatin by Intrinsic and Regulated Phase Separation. Cell **2019**, 179, 470-484.e21.
- 11. Nam, J.; Gwon, Y., Neuronal biomolecular condensates and their implications in neurodegenerative diseases. Front. aging neurosci. **2023**, 15.
- 12. Alberti, S.; Hyman, A. A., Biomolecular condensates at the nexus of cellular stress, protein aggregation disease and ageing. Nat. Rev. Mol. Cell Biol. **2021**, 22, 196-213.
- 13. Forenzo, C.; Larsen, J., Complex Coacervates as a Promising Vehicle for mRNA Delivery: A Comprehensive Review of Recent Advances and Challenges. Mol. Pharmaceutics **2023**, 20, 4387-4403.
- 14. Escalante, L. E.; Gasch, A. P., The role of stress-activated RNA-protein granules in surviving adversity. RNA (New York, N.Y.) **2021**, 27, 753-62.
- 15. Schütz, S.; Nöldeke, E. R.; Sprangers, R., A synergistic network of interactions promotes the formation of in vitro processing bodies and protects mRNA against decapping. Nucleic Acids Res. **2017**, 45, 6911-6922.
- 16. Boeynaems, S.; Alberti, S.; Fawzi, N. L.; Mittag, T.; Polymenidou, M.; Rousseau, F.; Schymkowitz, J.; Shorter, J.; Wolozin, B.; Van Den Bosch, L.; Tompa, P.; Fuxreiter, M., Protein Phase Separation: A New Phase in Cell Biology. Trends Cell Biol. **2018**, 28, 420-435.
- 17. Poudyal, R. R.; Pir Cakmak, F.; Keating, C. D.; Bevilacqua, P. C., Physical Principles and Extant Biology Reveal Roles for RNA-Containing Membraneless Compartments in Origins of Life Chemistry. Biochemistry **2018**, 57, 2509-2519.
- 18. Liu, J.; Tian, L.; Qiao, Y.; Zhou, S.; Patil, A. J.; Wang, K.; Li, M.; Mann, S., Hydrogel-Immobilized Coacervate Droplets as Modular Microreactor Assemblies. Angew. Chem. Int. Ed. **2020**, 59, 6853-6859.
- 19. Choi, S.; Meyer, M. O.; Bevilacqua, P. C.; Keating, C. D., Phase-specific RNA accumulation and duplex thermodynamics in multiphase coacervate models for membraneless organelles. Nat. Chem. **2022**, 14, 1110-1117.
- 20. Zhang, Y.; Chen, Y.; Yang, X.; He, X.; Li, M.; Liu, S.; Wang, K.; Liu, J.; Mann, S., Giant Coacervate Vesicles As an Integrated Approach to Cytomimetic Modeling. J. Am. Chem. Soc. **2021**, 143, 2866-2874.

- 21. Lu, T.; Spruijt, E., Multiphase Complex Coacervate Droplets. J. Am. Chem. Soc. 2020, 142, 2905-2914.
- 22. Lu, T.; Liese, S.; Schoenmakers, L.; Weber, C. A.; Suzuki, H.; Huck, W. T. S.; Spruijt, E., Endocytosis of Coacervates into Liposomes. J. Am. Chem. Soc. 2022, 144, 13451-13455.
- 23. Abbas, M.; Lipiński, W. P.; Nakashima, K. K.; Huck, W. T. S.; Spruijt, E., A short peptide synthon for liquid—liquid phase separation. Nat. Chem. **2021**, 13, 1046-1054.
- 24. Guindani, C.; da Silva, L. C.; Cao, S.; Ivanov, T.; Landfester, K., Synthetic Cells: From Simple Bio-Inspired Modules to Sophisticated Integrated Systems. Angew. Chem. Int. Ed. **2022**, 61, e202110855.
- 25. Li, P.; Banjade, S.; Cheng, H.-C.; Kim, S.; Chen, B.; Guo, L.; Llaguno, M.; Hollingsworth, J. V.; King, D. S.; Banani, S. F.; Russo, P. S.; Jiang, Q.-X.; Nixon, B. T.; Rosen, M. K., Phase transitions in the assembly of multivalent signalling proteins. Nature **2012**, 483 (7389), 336-340.
- 26. Cakmak, F. P.; Choi, S.; Meyer, M. O.; Bevilacqua, P. C.; Keating, C. D., Prebiotically-relevant low polyion multivalency can improve functionality of membraneless compartments. Nat. Commun. 2020, 11, 5949.
- 27. Owen, D. R.; Allerton, C. M. N.; Anderson, A. S.; Aschenbrenner, L.; Avery, M.; Berritt, S.; Boras, B.; Cardin, R. D.; Carlo, A.; Zhu, Y., An oral SARS-CoV-2 Mpro inhibitor clinical candidate for the treatment of COVID-19. Science 2021, 374, 1586-1593.
- 28. Jin, Z.; Du, X.; Xu, Y.; Deng, Y.; Liu, M.; Zhao, Y.; Zhang, B.; Li, X.; Zhang, L.; Yang, H., Structure of Mpro from SARS-CoV-2 and discovery of its inhibitors. Nature **2020**, 582, 289-293.
- 29. Jin, Z.; Mantri, Y.; Retout, M.; Cheng, Y.; Zhou, J.; Jorns, A.; Fajtova, P.; Yim, W.; Moore, C.; Xu, M.; Creyer, M. N.; Borum, R. M.; Zhou, J.; Wu, Z.; He, T.; Penny, W. F.; O'Donoghue, A. J.; Jokerst, J. V., A Charge-Switchable Zwitterionic Peptide for Rapid Detection of SARS-CoV-2 Main Protease. Angew. Chem. Int. Ed. **2022**, 61, e202112995.
- 30. Chang, Y.-C.; Jin, Z.; Li, K.; Zhou, J.; Yim, W.; Yeung, J.; Cheng, Y.; Retout, M.; Creyer, M. N.; Fajtová, P.; He, T.; Chen, X.; O'Donoghue, A. J.; Jokerst, J. V., Peptide valence-induced breaks in plasmonic coupling. Chem. Sci. **2023**, 14, 2659-2668.
- 31. Abbas, M.; Lipiński, W. P.; Wang, J.; Spruijt, E., Peptide-based coacervates as biomimetic protocells. Chem. Soc. Rev. **2021**, 50, 3690-3705.
- 32. Yang, M.; Digby, Z. A.; Chen, Y.; Schlenoff, J. B., Valence-induced jumps in coacervate properties. Sci. Adv. 2022, 8, eabm4783.
- 33. Viovy, J.-L., Electrophoresis of DNA and other polyelectrolytes: Physical mechanisms. Rev. Mod. Phys. **2000**, 72, 813-872.
- 34. Welsh, T. J.; Krainer, G.; Espinosa, J. R.; Joseph, J. A.; Sridhar, A.; Jahnel, M.; Arter, W. E.; Saar, K. L.; Alberti, S.; Collepardo-Guevara, R.; Knowles, T. P. J., Surface Electrostatics Govern the Emulsion Stability of Biomolecular Condensates. Nano Lett. **2022**, 22, 612-621.
- 35. Iglesias-Artola, J. M.; Drobot, B.; Kar, M.; Fritsch, A. W.; Mutschler, H.; Dora Tang, T. Y.; Kreysing, M., Chargedensity reduction promotes ribozyme activity in RNA-peptide coacervates via RNA fluidization and magnesium partitioning. Nat. Chem. **2022**, 14, 407-416.
- 36. Mason, A. F.; Buddingh', B. C.; Williams, D. S.; van Hest, J. C. M., Hierarchical Self-Assembly of a Copolymer-Stabilized Coacervate Protocell. J. Am. Chem. Soc. **2017**, 139, 17309-17312.
- 37. Bos, R.; Rutten, L.; van der Lubbe, J. E. M.; Bakkers, M. J. G.; Hardenberg, G.; Wegmann, F.; Zuijdgeest, D.; de Wilde, A. H.; Koornneef, A.; Verwilligen, A.; van Manen, D.; Kwaks, T.; Vogels, R.; Dalebout, T. J.; Myeni, S. K.; Kikkert, M.; Snijder, E. J.; Li, Z.; Barouch, D. H.; Vellinga, J.; Langedijk, J. P. M.; Zahn, R. C.; Custers, J.; Schuitemaker, H., Ad26 vector-based COVID-19 vaccine encoding a prefusion-stabilized SARS-CoV-2 Spike immunogen induces potent humoral and cellular immune responses. NPJ Vaccines 2020, 5, 91.
- 38. Wang, J.; Lin, C.-Y.; Moore, C.; Jhunjhunwala, A.; Jokerst, J. V., Switchable Photoacoustic Intensity of Methylene Blue via Sodium Dodecyl Sulfate Micellization. Langmuir **2018**, 34, 359-365.
- 39. Harms, M. J.; Castañeda, C. A.; Schlessman, J. L.; Sue, G. R.; Isom, D. G.; Cannon, B. R.; García-Moreno, E. B., The pK(a) values of acidic and basic residues buried at the same internal location in a protein are governed by different factors. J. Mol. Biol. **2009**, 389, 34-47.
- 40. Fitch, C. A.; Platzer, G.; Okon, M.; Garcia-Moreno, B. E.; McIntosh, L. P., Arginine: Its pKa value revisited. Protein Sci. 2015, 24, 752-61.
- 41. Jin, Z.; Li, Y.; Li, K.; Zhou, J.; Yeung, J.; Ling, C.; Yim, W.; He, T.; Cheng, Y.; Xu, M.; Creyer, M. N.; Chang, Y.-C.; Fajtová, P.; Retout, M.; Qi, B.; Li, S.; O'Donoghue, A. J.; Jokerst, J. V., Peptide Amphiphile Mediated Coassembly for Nanoplasmonic Sensing. Angew. Chem. Int. Ed. **2023**, 135, e202214394.

- 42. Vieregg, J. R.; Lueckheide, M.; Marciel, A. B.; Leon, L.; Bologna, A. J.; Rivera, J. R.; Tirrell, M. V., Oligonucleotide–Peptide Complexes: Phase Control by Hybridization. J. Am. Chem. Soc. **2018**, 140, 1632-1638.
- 43. Kumar Panigrahi, S.; Kumar Mishra, A., Inner filter effect in fluorescence spectroscopy: As a problem and as a solution. J. Photochem. Photobiol. C: Photochem. Rev. **2019**, 41, 100318.
- 44. Moore, C.; Borum, R. M.; Mantri, Y.; Xu, M.; Fajtová, P.; O'Donoghue, A. J.; Jokerst, J. V., Activatable Carbocyanine Dimers for Photoacoustic and Fluorescent Detection of Protease Activity. ACS Sens. **2021**, 6, 2356-2365.
- 45. Li, L.; Srivastava, S.; Andreev, M.; Marciel, A. B.; de Pablo, J. J.; Tirrell, M. V., Phase Behavior and Salt Partitioning in Polyelectrolyte Complex Coacervates. Macromolecules **2018**, 51, 2988-2995.
- 46. Yim, W.; Zhou, J.; Sasi, L.; Zhao, J.; Yeung, J.; Cheng, Y.; Jin, Z.; Johnson, W.; Xu, M.; Palma-Chavez, J.; Fu, L.; Qi, B.; Retout, M.; Shah, N. J.; Bae, J.; Jokerst, J. V., 3D-Bioprinted Phantom with Human Skin Phototypes for Biomedical Optics. Adv. Mater. 2023, 35, 2206385.
- 47. Jin, Z.; Ling, C.; Li, Y.; Zhou, J.; Li, K.; Yim, W.; Yeung, J.; Chang, Y.-C.; He, T.; Cheng, Y.; Fajtová, P.; Retout, M.; O'Donoghue, A. J.; Jokerst, J. V., Spacer Matters: All-Peptide-Based Ligand for Promoting Interfacial Proteolysis and Plasmonic Coupling. Nano Lett. **2022**, 22, 8932-8940.
- 48. Zhang, L.; Lin, D.; Sun, X.; Curth, U.; Drosten, C.; Sauerhering, L.; Becker, S.; Rox, K.; Hilgenfeld, R., Crystal structure of SARS-CoV-2 main protease provides a basis for design of improved ketoamide inhibitors. Science **2020**, 368, 409-412.
- 49. Jin, Z.; Dridi, N.; Palui, G.; Palomo, V.; Jokerst, J. V.; Dawson, P. E.; Sang, Q.-X. A.; Mattoussi, H., Quantum Dot–Peptide Conjugates as Energy Transfer Probes for Sensing the Proteolytic Activity of Matrix Metalloproteinase-14. Anal. Chem. **2023**, 95, 2713-2722.
- 50. Jin, Z.; Dridi, N.; Palui, G.; Palomo, V.; Jokerst, J. V.; Dawson, P. E.; Amy Sang, Q.-X.; Mattoussi, H., Evaluating the Catalytic Efficiency of the Human Membrane-type 1 Matrix Metalloproteinase (MMP-14) Using AuNP-Peptide Conjugates. J. Am. Chem. Soc. **2023**, 145, 4570-4582.
- 51. Sun, H.; Qiao, B.; Choi, W.; Hampu, N.; McCallum, N. C.; Thompson, M. P.; Oktawiec, J.; Weigand, S.; Ebrahim, O. M.; de la Cruz, M. O.; Gianneschi, N. C., Origin of Proteolytic Stability of Peptide-Brush Polymers as Globular Proteomimetics. ACS Cent. Sci. **2021**, 7, 2063-2072.
- 52. Algar, W. R.; Malonoski, A.; Deschamps, J. R.; Blanco-Canosa, J. B.; Susumu, K.; Stewart, M. H.; Johnson, B. J.; Dawson, P. E.; Medintz, I. L., Proteolytic Activity at Quantum Dot-Conjugates: Kinetic Analysis Reveals Enhanced Enzyme Activity and Localized Interfacial "Hopping". Nano Lett. **2012**, 12, 3793-3802.
- 53. Armbruster, D. A.; Pry, T., Limit of blank, limit of detection and limit of quantitation. Clin. Biochem. Rev. **2008**, 29 Suppl 1, S49-S52.
- 54. Henderson, P. J., A linear equation that describes the steady-state kinetics of enzymes and subcellular particles interacting with tightly bound inhibitors. Biochem. J. 1972, 127, 321-333.
- 55. Hurst, D. R.; Schwartz, M. A.; Ghaffari, M. A.; Jin, Y.; Tschesche, H.; Fields, G. B.; Sang, Q.-X. A., Catalytic- and ecto-domains of membrane type 1-matrix metalloproteinase have similar inhibition profiles but distinct endopeptidase activities. Biochem. J. **2004**, 377, 775-779.
- 56. Lu, J.; Chen, S. A.; Khan, M. B.; Brassard, R.; Arutyunova, E.; Lamer, T.; Vuong, W.; Fischer, C.; Young, H. S.; Vederas, J. C.; Lemieux, M. J., Crystallization of Feline Coronavirus Mpro With GC376 Reveals Mechanism of Inhibition. Front. Chem. **2022**, 10, 852210.
- 57. Jin, Z.; Jorns, A.; Yim, W.; Wing, R.; Mantri, Y.; Zhou, J.; Zhou, J.; Wu, Z.; Moore, C.; Penny, W. F.; Jokerst, J. V., Mapping Aerosolized Saliva on Face Coverings for Biosensing Applications. Anal. Chem. **2021**, 93, 11025-11032
- 58. Zhou, J.; Yim, W.; Zhou, J.; Jin, Z.; Xu, M.; Mantri, Y.; He, T.; Cheng, Y.; Fu, L.; Jokerst, J. V., A fiber optic photoacoustic sensor for real-time heparin monitoring. Biosens. Bioelectron. **2022**, 196, 113692.
- 59. Black, K. A.; Priftis, D.; Perry, S. L.; Yip, J.; Byun, W. Y.; Tirrell, M., Protein Encapsulation via Polypeptide Complex Coacervation. ACS Macro Lett. 2014, 3, 1088-1091.
- 60. Kaman, W. E.; Galassi, F.; de Soet, J. J.; Bizzarro, S.; Loos, B. G.; Veerman, E. C.; van Belkum, A.; Hays, J. P.; Bikker, F. J., Highly specific protease-based approach for detection of porphyromonas gingivalis in diagnosis of periodontitis. J. Clin. Microbiol. **2012**, 50, 104-12.